buildings

MDPI

Article

Utilization of Copper–Molybdenum Tailings to Enhance the Compressive Strength of Alkali-Activated Slag-Fly Ash System

Fengdan Wang [1,2,3], Xiaowei Gu [1,2,3,*], Qing Wang [1,2,3], Jianping Liu [4], Xiaochuan Xu, [1,2,3] and Yunqi Zhao [1,2,3]

[1] School of Resources and Civil Engineering, Northeastern University, Shenyang 110819, China; 2290114@stu.neu.edu.cn (F.W.); wangqing1@mail.neu.edu.cn (Q.W.); xuxiaochuan@mail.neu.edu.cn (X.X.); 1810399@stu.neu.edu.cn (Y.Z.)
[2] Science and Technology Innovation Center of Smart Water and Resource Environment, Northeastern University, Shenyang 110819, China
[3] Liaoning Institute of Technological Innovation in Solid Waste Utilization, Shenyang 110819, China
[4] School of Architecture and Civil Engineering, Shenyang University of Technology, Shenyang 110870, China; liujianping024@163.com
* Correspondence: guxiaowei@mail.neu.edu.cn

Abstract: Utilizing a variety of solid wastes to prepare alkali-activated cementitious materials is one of the principal trends in the development of cementitious materials. Commonly used alkali activation precursors such as granulated blast furnace slag (GBFS) and fly ash (FA) will be less available due to resource pressures. Supply limitation is an important reason to research alternative precursors. To realize the high value-added utilization of copper–molybdenum tailings (CMTs), this study adopted the modified sodium silicate solution as an alkaline activator to activate GBFS-FA-CMTs cementitious system to prepare alkali-activated cementitious materials. The influence of CMTs content on the compressive strength of GBFS-FA-CMTs cementitious system was analyzed, and the mechanism of GBFS-FA-CMTs cementitious system was also analyzed through hydration product types, physical phase composition, and microscopic morphology. The results indicated that a paste with the incorporation of CMTs, S50F30C20 (50% GBFS, 30% FA, 20% CMTs), achieved the highest compressive strength of 79.14 MPa, which was due to the filling effect of the CMTs and the degree of participation in the reaction. Pastes with different contents of CMTs, while maintaining a constant CBFS content, exhibited similar strength development. Excessive amounts of CMTs could result in reduced compressive strength. Microstructural analysis revealed that the hydration products were structurally altered by the addition of CMTs. In addition to ettringite, quartz, C(-N)-S-H gel, and calcite, gaylussite was also formed; moreover, the mass of chemically bound water increased, and the microstructure of reaction products became denser. An excess of CMTs may restrict the growth of the hydration gel, leading to more microstructural defects. The study suggests that CMTs could enhance the compressive strength of hardened paste within an alkali-activated slag-fly ash system, possibly due to a filling effect and participation in the chemical reaction. This research confirms the feasibility of using CMTs in alkali-activated cementitious materials.

Keywords: alkali activation; copper–molybdenum tailings; compressive strength; microstructure

Citation: Wang, F.; Gu, X.; Wang, Q.; Liu, J.; Xu, X.; Zhao, Y. Utilization of Copper–Molybdenum Tailings to Enhance the Compressive Strength of Alkali-Activated Slag-Fly Ash System. *Buildings* **2024**, *14*, 1031. https://doi.org/10.3390/buildings14041031

Academic Editor(s): Xiaoyong Wang

Received: 16 February 2024
Revised: 13 March 2024
Accepted: 22 March 2024
Published: 7 April 2024

1. Introduction

Cement plays an indispensable role in the construction industry and is one of the main materials for buildings [1]. Data indicate that the global annual production of cement was as high as 4 billion tons [2]; in particular, the annual production of cement in China accounted for 51.17% of the global annual production [3]. It was projected that by 2050, the annual production of cement will increase to about 6 billion tons [4]. However, the production of cement emits carbon dioxide and other gases that contribute to environmental pollution. [5]. Specifically, carbon dioxide emission during cement production

primarily originated from the production of clinker [6]. Statistics show that the production of one ton of cement clinker results in the emission of 0.9 to 1 ton of carbon dioxide [5], with the global cement industry contributing to 8% of total carbon emissions [7], causing severe environmental pollution. Moreover, large amounts of energy, raw materials, and resources are consumed in the production of cement [8]. Energy consumption for cement production has been reported to be about 110–120 kilowatt-hours per ton, accounting for a considerable proportion of the total industrial energy consumption [9]. Therefore, the high pollution and high energy consumption of cement production make it an urgent task to find alternative green building materials.

On the other hand, as the industrialization process of countries accelerates, a large amount of industrial solid waste accumulates without effective utilization [10]. Mine tailings, as a kind of industrial solid waste produced after mineral beneficiation and the recovery of ores, are also increasing in both storage and emission volumes [11]. The storage of mine tailings occupies a significant amount of land resources, and tailings dams may pose risks of secondary disasters such as landslides and debris flows, threatening the safety of surrounding areas [12,13]. Tailings may contain heavy metals, harmful chemicals, and other pollutants, which can be released into the environment, causing pollution to soil, water, and air [14]. However, not all components of mine tailings are harmful; valuable metal elements in the tailings could be recycled and reused [15]. Most mine tailings contain minerals such as aluminum, calcium, and silicates, which could be used to develop related building material products [16,17]. Thus, the resource utilization of tailings and the development of related building materials are key to addressing resource waste and environmental pollution.

Alkali-activated materials (AAMs) have alleviated the environmental pollution issues associated with cement [18,19]. AAMs consist of an alkali activator and a precursor [20], with similar compressive strength and durability properties to Portland cement [21]. Commonly used alkali activation precursors such as GBFS and FA will be less available due to resource pressures. Supply limitation is an important reason to research alternative precursors [22]. AAMs could consume vast quantities of industrial solid waste such as FA, iron ore tailings, and GBFS [23–25] and save up to 14% of the cost of replacing precursors and activators with industrial residues [26], making them one of the most promising green cementitious materials [27,28]. In previous studies on industrial solid waste as AAMs precursors, the most common were GBFS, FA, metakaolin, and tailings [21,29]. Some studies indicated that GBFS prepared cementitious materials with compressive strengths comparable to Portland cement [30]. AAMs prepared from finely ground electric arc furnace stainless steel slag (EAFSS) and ground GBFS had reduced the heat of hydration released by the paste, positively influencing the paste properties, extending the setting time, and achieving a compressive strength value exceeding 85 MPa at a 1:1 mass ratio of EAFSS to ground GBFS after 28 days [31]. Additionally, the mechanical properties and durability of AAMs might be affected by different environmental and curing conditions [32].

Utilizing synergistic effects between GBFS and other types of industrial solid wastes could lead to the production of high-performance, environmentally friendly construction materials [22]. A synergistic effect was exhibited within an alkaline environment between GBFS and red mud; when GBFS was partially replaced by red mud, its mechanical properties were comparable to or better than those samples without added red mud [33]. AAMs prepared using GBFS, FA, and limestone demonstrate that the raw material components of FA and limestone had a minuscule impact on compressive strength, with the reaction process predominantly controlled by blast furnace slag [34]. The investigation found that the microstructure of AAMs developed from mechanically treated tailings became denser and more uniform, resulting in an increased compressive strength [35]. Research indicated that submicron mine tailings particles play the role of fillers as precursors and that the reaction process can be accelerated to improve the microstructure of alkali-activated pastes [36]. Furthermore, Tian et al. [37] pointed out that prepared AAMs with 90% mass of copper tailings and 10% mass of FA as precursors increased the compressive

strength of AAMs. Research by [38] also reached similar conclusions. Geopolymer composites prepared from copper tailings demonstrated excellent mechanical properties [39]. Wang et al. [40] adopted the copper tailings–GBFS system, and the compressive strength was increased by 5.5–19.8% at 28 d. Molybdenum tailings and GBFS were used to prepare a one-part geopolymer, and the compressive strength of the geopolymer reached 44 MPa at 28 d with 80% slag content [41]. Copper tailings can be used as raw materials and additives to produce cement [42]. Alkali-activated molybdenum tailings were used to produce ecological Ultra High-Performance Composites [43], which provided a new application in recycling industrial solid wastes.

Although the effects of various mine tailings on the properties and hydration mechanisms of alkali-activated cementitious materials have been investigated, relatively few studies have been conducted on the use of CMTs to replace GBFS and FA in the preparation of cementitious materials. To realize the high value-added utilization of CMTs, alkali-activated cementitious materials were prepared with GBFS, FA, CMTs, and modified sodium silicate solution as the main raw materials in this study. CMTs were used as a calcium source to provide the activated calcium required for the alkali-activated system. The influence of CMTs content on the compressive strength of the alkali-activated GBFS-FA-CMTs system (AASFCS) was analyzed. The physical composition and microstructure of the hydration products were characterized using X-ray diffraction (XRD), Fourier transform infrared spectroscopy (FTIR), scanning electron microscopy-energy spectroscopy (SEM-EDS), and thermos-gravimetric and derivative thermos-gravimetric (TG-DTG). This study can reduce the environmental pollution caused by industrial solid waste and cement production and provide a basis for the optimization of the mechanical properties of CMTs alkali-activated cementitious materials.

2. Materials and Methods

2.1. Materials

The experimental raw materials of this study were finely ground GBFS, FA, and CMTs. The CMTs are solid waste generated from the flotation extraction of copper and molybdenum concentrates from copper–molybdenum ore. The LOI of CMTs, GBFS, and FA were 7.45%, 0.84%, and 2.37%, respectively. The 28 d activity index of CMTs, GBFS, and FA were 68.26%, 98.50%, and 84.20%, respectively. The chemical composition and XRD patterns of GBFS, FA, and CMTs are shown in Table 1 and Figure 1, respectively.

Table 1. Main chemical compositions of GBFS, FA, and CMTs.

Oxides (wt.%)	GBFS	FA	CMTs
SiO_2	31.98	60.24	28.42
CaO	36.91	2.49	41.52
Al_2O_3	17.22	29.38	4.41
K_2O	1.60	1.24	1.37
Fe_2O_3	0.62	3.78	11.01
MgO	9.27	0.50	1.39
SO_3	1.81	0.26	0.91
MnO	0.12	0.05	0.95

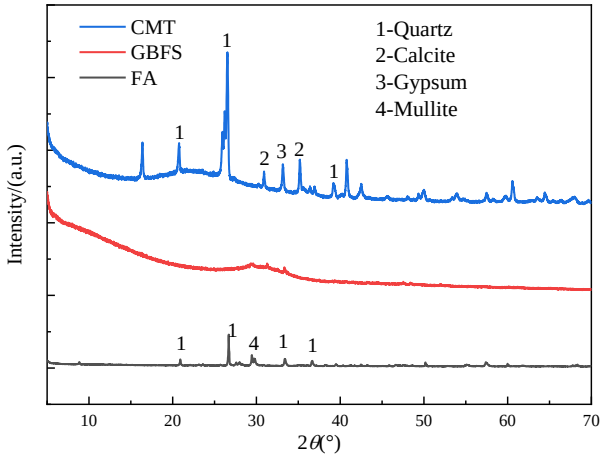

Figure 1. XRD patterns of GBFS, FA, and CMTs.

The median particle size (D50) of the CMTs was 282.7 μm, indicating a relatively coarse granularity. Hence, the copper–molybdenum tailings used in this study were mechanically milled for 10 min. The particle size distribution of the milled CMTs, measured using a Bettersizer 2600 particle size analyzer, is depicted in Figure 2, with a post-milling median particle size (D50) of 6.28 μm. The activator used was a modified sodium silicate solution, prepared by adding an appropriate amount of sodium hydroxide particles (analytical level) to the sodium silicate solution with the modulus (Ms, SiO_2/Na_2O molar ratio) of 3.3. The modified sodium silicate solution was returned to room temperature and adjusted to the desired water–solid ratio by adding distilled water, and the solution was stored for 24 h.

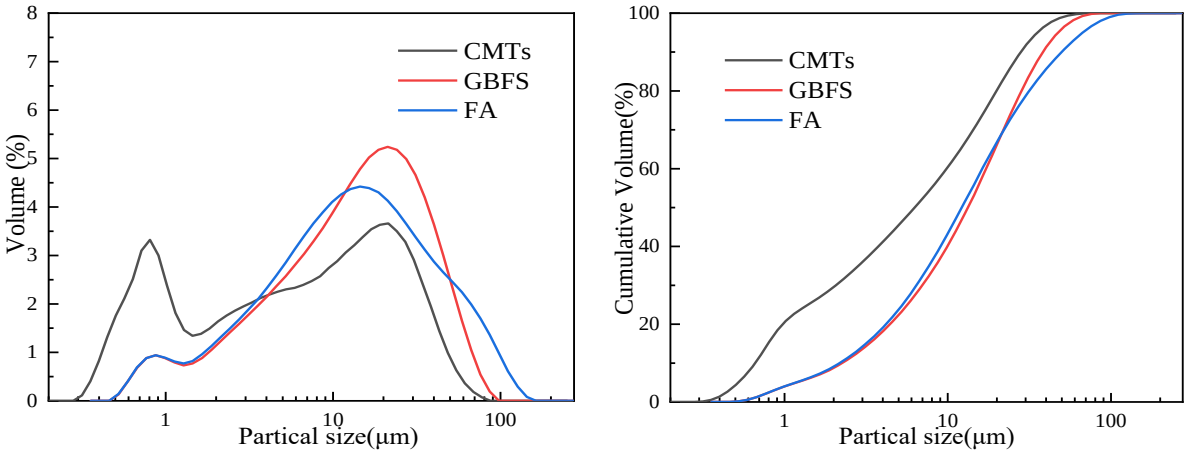

Figure 2. Particle size distribution of ground CMTs, GBFS, and FA: (**a**) incremental particle size distribution; (**b**) cumulative particle size distribution.

2.2. Sample Preparation

To analyze the impact of CMTs on the compressive strength of AASFCS, the hardened paste was prepared. Based on the principle of providing sufficient alkalinity without efflorescence [10] and based on preliminary studies, the modulus of the activator was determined to be 1.2. The mass ratio of the modified sodium silicate solution to the total mass of the solution in the mixture, which represents the activator mass concentration (Mc), was fixed at 45%. Three levels of slag content were used—50%, 40%, and 30% by mass [44–46]—along with CMTs additions ranging from 0% to 50%, and the liquid-to-

solid ratio was maintained at 0.4. Detailed information regarding the mix proportions can be found in Table 2.

The hardened paste was prepared in a paste mixer; GBFS, FA, and CMTs were mixed in the mixer, and then pre-prepared modified sodium silicate solution was added. All components were combined at low speed for 30 s, paused for 30 s, and then mixed at high speed for 120 s. The fresh paste would be poured into 40 × 40 × 40 mm plastic molds and vibrated for 60 s before being covered with transparent film on the surface of the mold for 24 h. Subsequently, all samples were demolded and cured to test age at 20 ± 2 °C and 95% relative humidity. Figure 3 illustrates the preparation and microstructural examination process of the prisms.

Figure 3. Pictures of the plastic molds.

Table 2. Mixture proportions of samples.

	Activator	Solid Raw Materials					
		GBFS (wt%)	FA (wt%)	CMTs (wt%)	GBFS (kg/m³)	FA (kg/m³)	CMTs (kg/m³)
S50F50C0		50	50		150	150	
S40F60C0		40	60	0	120	180	0
S30F70C0		30	70		90	210	
S50F40C10		50	40		150	120	
S40F50C10		40	50	10	120	150	30
S30F60C10		30	60		90	180	
S50F30C20		50	30		150	90	
S40F40C20		40	40	20	120	120	60
S30F50C20	Ms [1] = 1.2	30	50		90	150	
S50F20C30	Mc [2] = 45%	50	20		150	60	
S40F30C30		40	30	30	120	90	90
S30F40C30		30	40		90	120	
S50F10C40		50	10		150	30	
S40F20C40		40	20	40	120	60	120
S30F30C40		30	30		90	90	
S50F0C50		50	0		150	0	
S40F10C50		40	10	50	120	30	150
S30F20C50		30	20		90	60	

[1] Modulus, [2] Mass concentration.

2.3. Testing Methods

According to Chinese Standard GB/T 17671-2021 [47], the specimen size was determined as 40 mm × 40 mm × 40 mm; a picture of the plastic molds is shown in Figure 3. A constant-load compression testing machine was used for the 28 d age compressive

strength test; the loading speed was 2.4 kN/s. Each mix proportion consisted of two specimens, and the average of the test results would be used as the final compressive strength for that group. If one of the test results was greater or less than 15% of the mean, the group failed, and the experiment was repeated.

After the compressive strength test was completed, fragments from the middle part of the specimen were soaked in anhydrous ethanol for 24 h to abort hydration; then the specimen fragments were dried in 40 °C oven for 24 h. The dried specimen fragments were ground and passed through a −75μm sieve, and 10mg was taken for XRD analysis, with a test range of 10° to 75° and a scanning speed of 5°/min., 10mg of the same sample is used for TG-DTG analysis, with a test temperature range of 30 °C to 1000 °C and a heating rate of 20 °C/min. Next, 1 mg of the dried sample was thoroughly ground with 100 mg of pure KBr in an agate mortar, pressed into a disc, and then analyzed using Fourier-transform infrared spectroscopy, with a wavenumber range of 4000–400 cm^{-1}.

A scanning electron microscope, model ZEISS Sigma 500, could be used to analyze morphological variations in the microstructure of hydration products in the sample. After the compressive strength test, thin flake-like sample fragments are selected, soaked in anhydrous ethanol, and dried in 40 °C oven for 24 h, then fixed on an aluminum plate with conductive tape for gold sputtering to observe and analyze the microscopic morphology of the hardened paste and to perform EDS analysis. Figure 4 shows the preparation and microanalysis process of AASFCS.

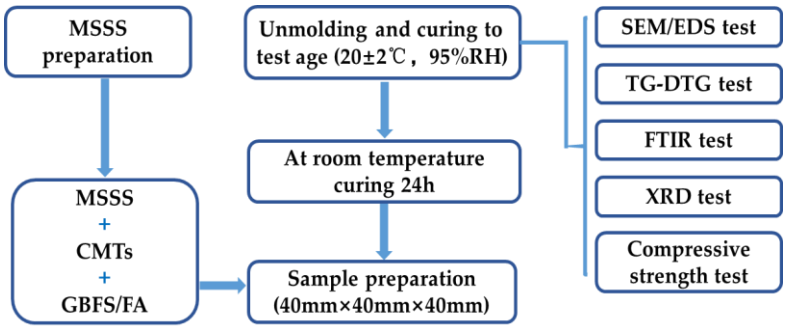

Figure 4. Experimental processes for AASFCS.

3. Results and Discussion

3.1. Compressive Strength

After 28 days of curing, the compressive strength of the AASFCS paste mixtures was presented in Figure 5. The data indicated that the samples exhibited a similar trend in the development of compressive strength when the GBFS content was at 50%, 40%, and 30%. With a constant GBFS content, an increase in CMTs content from 0% to 20% resulted in an increase in compressive strength at 28 days. For example, in samples with 50% GBFS content, an increase in CMTs from 0% to 20% enhanced the 28 d compressive strength from 74.8 MPa to 79.14 MPa. Similar results were observed for samples with 40% and 30% GBFS content, with the 20% CMTs content samples exhibiting the highest compressive strength. Excess CMTs could lead to reduced compressive strength. This outcome might be attributed to the filling effect of CMTs, from which the addition of CMTs increased the fine particle content in the mixture (as shown in Figure 2), leading to a denser sample structure. Additionally, the fine particles of CMTs provided extra activation sites which promote the formation of reaction products, thereby enhancing strength. Furthermore, the reaction between CMTs and the modified sodium silicate solution might increase the variety of reaction products and alter the structure of the reaction products, resulting in changes in compressive strength.

It could be seen that when the content of CMTs was held constant, the compressive strength of the specimens increased with the increase in the amount of CBFS. For instance,

with 0% CMTs content, when the CBFS content was reduced from 50% to 30%, the 28 d compressive strength decreased from 74.8 MPa to 34.15 MPa. When the CMTs content was at 20%, the samples for each CBFS content level reached their maximum compressive strength. Existing research has demonstrated the significant impact of CBFS content on the compressive strength of the alkali-activated system, affecting both the setting time and the reaction process [48]. Under the condition of constant CBFS content, varying the amounts of FA and CMTs influences the compressive strength of the samples by only 8%–20%, while samples with different CMTs contents exhibited similar strength development. Considering the increase in CMTs content alongside a decrease in FA content, it seems FA retained a low reactivity after 28 days of curing at room temperature.

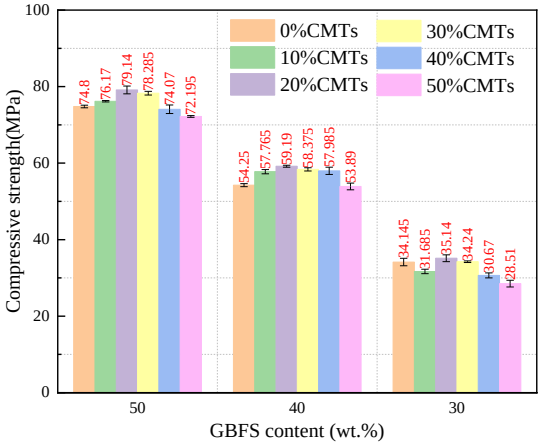

Figure 5. Compressive strength of AASFCS cured for 28 d.

3.2. XRD Analysis

The XRD patterns of the 28-day cured AASFCS paste mixtures (with 50% GBFS content) are shown in Figure 6. The changes in the crystalline peaks of the reaction products in the samples were related to the content of FA and CMTs in the AASFCS. The main mineral phases in sample S50F50C0 were ettringite, quartz, C(-N)-S-H gel, and calcite [49], while the samples with added CMTs exhibit the presence of the complex salt phase $CaNa_2(CO_3)_2$. Gaylussite ($CaNa_2(CO_3)_2 \cdot 5H_2O$) could be observed in the XRD pattern at approximately $2\theta = 36.2°$ [50]. The presence of gaylussite implies the dissolution of Ca^{2+} from CMTs under alkaline conditions, suggesting that hydration of CMTs may occur in the presence of alkali. The $CaCO_3$ in CMTs may interact with Na+, with Na+ partially substituting the calcium ions in the crystal structure of calcium carbonate, forming a new complex salt crystal of $CaNa_2(CO_3)_2$. This substitution results in Ca^{2+} and Na^+ occupying the octahedral voids between $[CO_3]^{2-}$, leading to a denser structure.

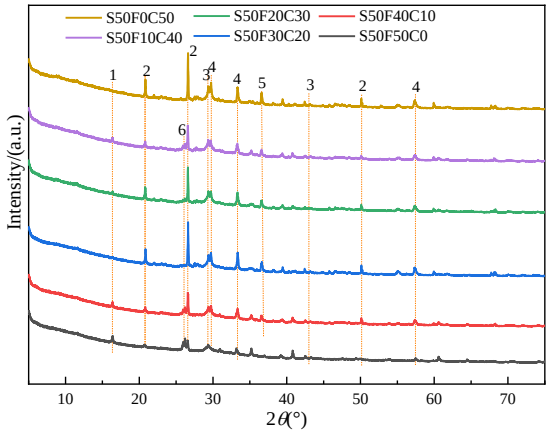

Figure 6. XRD patterns of AASFCS cured for 28 d. (1—Ettringite，2—Quartz, 3—C(-N)-S-H gel, 4—Calcite, 5—Gaylussite, 6—Mullite).

3.3. FTIR Analysis

After curing for 28 days, the AASFCS (50% GBFS) were characterized by FTIR spectroscopy (Figure 7). The spectra of different samples showed similar curves, with major vibrational bands at 3448 cm^{-1}, 1645 cm^{-1}, 1428 cm^{-1}, 990 cm^{-1}, 970 cm^{-1}, 875 cm^{-1}, and 450 cm^{-1}. Post-alkali activation, the absorption peaks at 3448 cm^{-1} and 1645 cm^{-1} corresponded to the bending and stretching vibrations of H-O-H and O-H [31], respectively, confirming the presence of crystalline water in the hydration products of AASFCS. The bands at 1428 cm^{-1} and 875 cm^{-1} were attributed to the asymmetric stretching and bending vibrations of O-C-O in carbonates [31], indicating a significant increase in the intensity of the CO_3^{2-} group absorption band with an increase in the copper–molybdenum tailings content. The bands at 990 cm^{-1} and 970 cm^{-1} correlated to the asymmetric stretching vibrations of Si-O-Si or Si-O-Al [51], suggesting that the major hydration product was the C(-N)-S-H gel. The shift in these band positions confirmed changes in the structure of the hydration products, consistent with XRD results. The absorption peak at 450 cm^{-1} was due to the bending vibrations of Si-O and Al-O [51]. Given the limited information on the composition of hydration products provided by FTIR, further analysis was conducted using EDS to more precisely differentiate the composition of the hydration products.

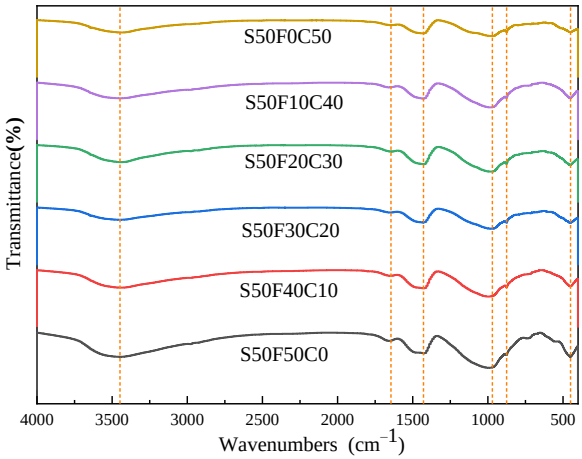

Figure 7. FTIR spectra of AASFCS cured for 28 d.

3.4. TG Analysis

Figure 8 presented the TG and DTG curves of the AASFCS paste mixtures with a GBFS content of 50% after 28 days of curing. As can be observed from Figure 8, there were three main weight loss peaks in the cured paste mixture samples, with the first and third peaks being more pronounced. Specifically, significant weight loss occurred between 100–200 °C and 700–800 °C, which was similar to the analysis results of the study by [4]. The weight loss peaks in the mixtures containing CMTs were more pronounced compared to the S50F50C0 sample.

The weight loss peak between 100 and 200 °C, occurring around 130 °C, was attributed to the evaporation of free water and dehydration of the C-S-H gel [52]. The second weight loss region, between 450 and 550 °C with a peak around 540 °C, was due to the dehydration of the C(-A)-S-H gel [53], which was present in smaller quantities in the samples, consistent with the analysis results from XRD and FTIR. As the temperature continued to rise, the third weight loss region appeared between 700 and 800 °C, with the peak concentrated around 750 °C, primarily due to the decomposition of carbonates [54].

To investigate the impact of incorporating CMTs on the reaction products, the content of physically bound water (PBW) and chemically bound water (CBW) in the samples was

calculated based on the TG-DTG results, as shown in Figure 9. The PBW content of the samples was calculated based on the mass loss before 105 °C, while the CBW content was determined by the dehydration mass loss between 105 °C and 200 °C [34]. The addition of CMTs generally resulted in a decrease in the content of physically bound water, but an increasing trend in the mass of chemically bound water in the samples was observed. The possible explanation for this phenomenon could be found in the XRD results, which indicate that the addition of CMTs leads to the generation of additional hydration products; hence the increase in chemically bound water. On one hand, this might be due to the fine particles in CMTs providing additional nucleation sites that enhance the hydration product formation and reduce porosity, leading to a slight increase in the amount of chemically bound water. On the other hand, it might be due to the Ca^{2+} ions released from CMTs under the action of alkaline solutions.

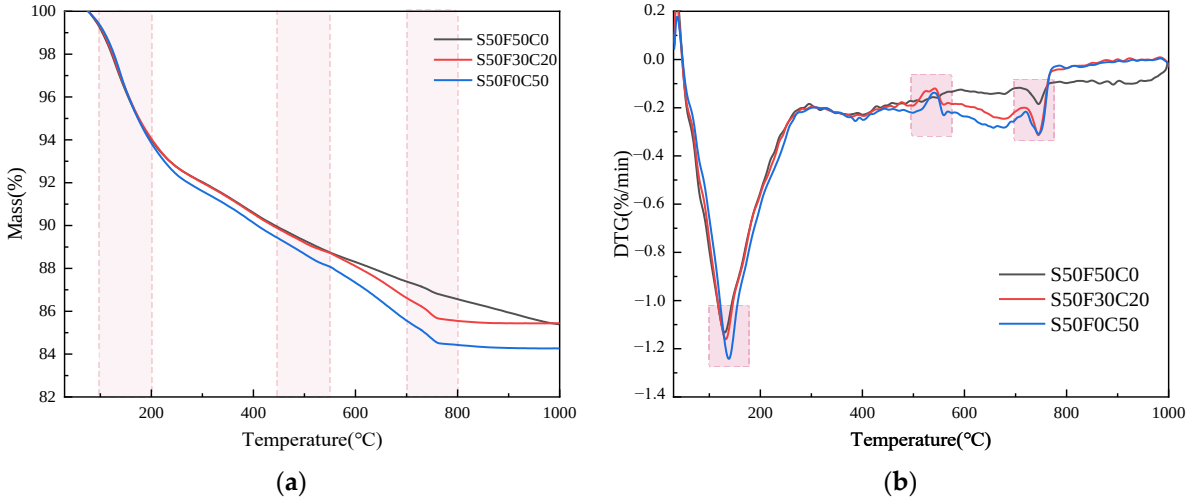

Figure 8. TG-DTG analysis of AASFCS cured for 28 d: (**a**) TG analysis; (**b**) DTG analysis.

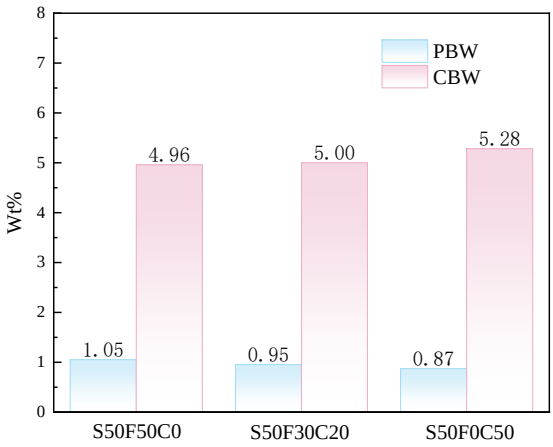

Figure 9. Mass fraction of PBW and CBW in AASFCS cured for 28 d.

3.5. SEM/EDS Analysis

To further clarify the influence of the copper–molybdenum tailings dosage on the composition and microstructure of the hydration products in the AASFCS paste mixtures, SEM and EDS spot scans were performed on the samples after 28 days of curing. The micro-morphology of the samples S50F50C0, S50F30C20, S50F0C50, and S50F30C20 is shown in Figure 10a–d. It was noteworthy that the presence of CMTs significantly affected the morphological characteristics of the hydration products.

As shown in Figure 10a, a certain amount of flake-like and chain-like hydration products could be directly observed. The hydration products were mainly C-S-H, C(-A)-S-H, and C(-N)-S-H. The calcium and aluminum components from GBFS and FA participate in the reaction to form C(-A)-S-H. The spherical particles of fly ash were surrounded by hydration products, which provided compressive strength to the samples. However, some unreacted intact spherical FA particles were still visible, with numerous pores formed between the hydration products and the unreacted particles, and microcracks were also present between the hydration products. Figure 10b,d depict the microstructure of the mixture samples with 20% CMTs added, with the main type of hydration product being C(-A)-S-H, among others. The FA particles enwrapped by hydration products could be directly observed. Notably, there was also a large amount of three-dimensional block-like products in the mixture samples, which were gaylussite ($CaNa_2(CO_3)_2 \cdot 5H_2O$) formed in solutions with lower Na^+ concentration, consistent with the XRD results. Compared to the S50F50C0 sample in Figure 10a, the unreacted raw material particles were hardly visible in Figure 10d. FA and GBFS participated sufficiently in the hydration reaction to form silicate gels. FA spheres wrapped in gaylussite with silicate gels to form a continuous whole. Due to the addition of CMTs, microdefects such as micropores and cracks were significantly reduced, resulting in a denser microstructure. This dense and compact structure was conducive to achieving higher compressive strength. Figure 10c showed the sample with 50% CMTs added, with the main hydration products being C-S-H and gaylussite ($CaNa_2(CO_3)_2 \cdot 5H_2O$). The excess CMTs particles seemed to limit the growth of the hydration gel, leading to poorer continuity and more microdefects in the sample, hence exhibiting lower compressive strength.

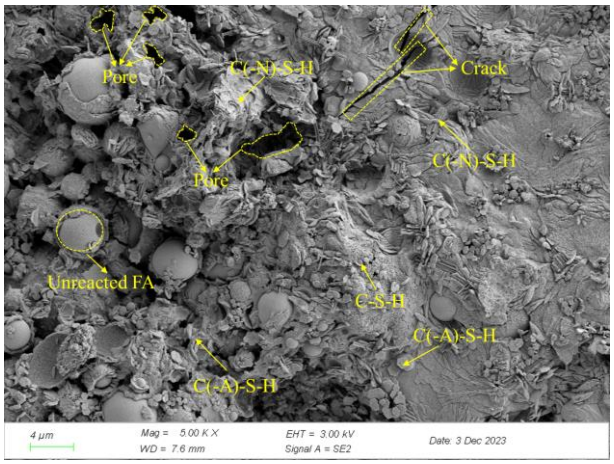

(**a**)

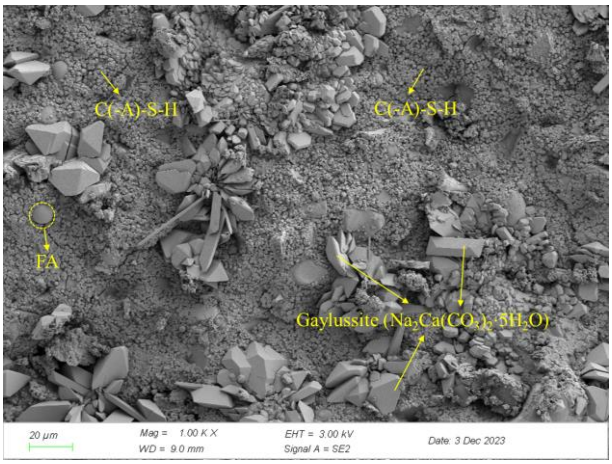

(**b**)

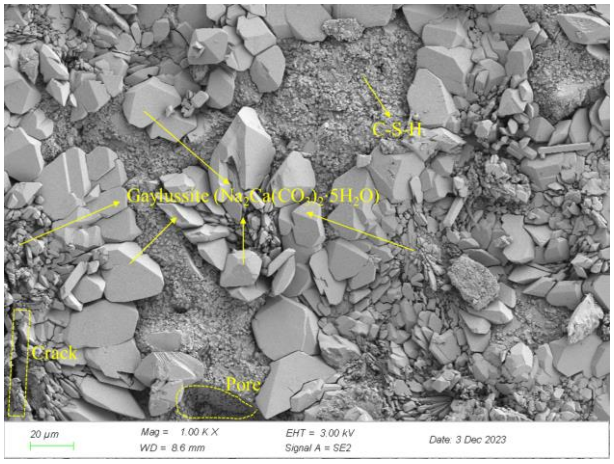

(**c**)

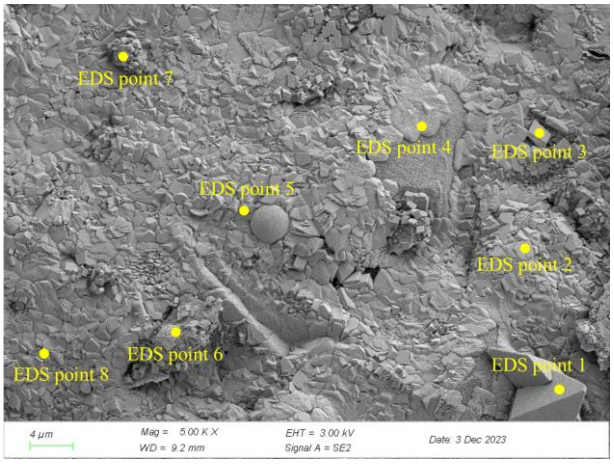

(**d**)

Figure 10. SEM images of AASFCS cured for 28 d: (**a**) Sample S50F50C0; (**b**) Sample S50F30C20; (**c**) Sample S50F0C50; (**d**) Sample S50F30C20.

Figure 11 presents the EDS results of the elements Ca, Si, Mg, Al, Fe, and O in the sample S50F30C20 from Figure 10d. The composition of the elements Ca, Si, Mg, Al, Fe, and O in the microstructure of the sample S50F50C0 from Figure 10a is shown in Figure 12. The Ca/Si atomic ratio of the hydration products of sample S50F30C20 were calculated to be in the range of 1.8 to 2.3, which was slightly higher than the data reported in existing studies [50,55]. The Ca/Si atomic ratio of the hydration products in sample S50F50C0 was 0.8, which was consistent with the data from current research. Figure 13 illustrated the Ca/Si and Ca/Al atomic ratios of sample S50F30C20, sample S50F50C0, and the raw materials. The changes in the content of Ca in the hydration products of the samples induced by the addition of CMT were analyzed in comparison.

The incorporation of CMTs significantly increased the Ca/Si atomic ratio in the hydration products of the samples. This phenomenon was primarily due to the chemical composition differences of the CMTs. Although the relationship between the Ca/Si ratio and compressive strength was not yet clear, a higher Ca/Si atomic ratio contributes to suppressing the drying shrinkage of the samples and further improves the continuity of the microstructure [56], which aligned with the results of the SEM microstructure analysis. EDS results indicated that the atomic percentage of Na in the structure of hydration products varies between 0.91% and 15.67%. The Ca/Na atomic ratio in sample S50F30C20 was 0.92–16.23, an increase compared to the 0.71 ratio in S50F50C0, suggesting that the addition of CMTs promotes the development of C(-A)-S-H, consistent with the XRD test results. The EDS results also showed that the Al/Ca atomic ratio in sample S50F30C20 ranges from 0.12 to 0.54.

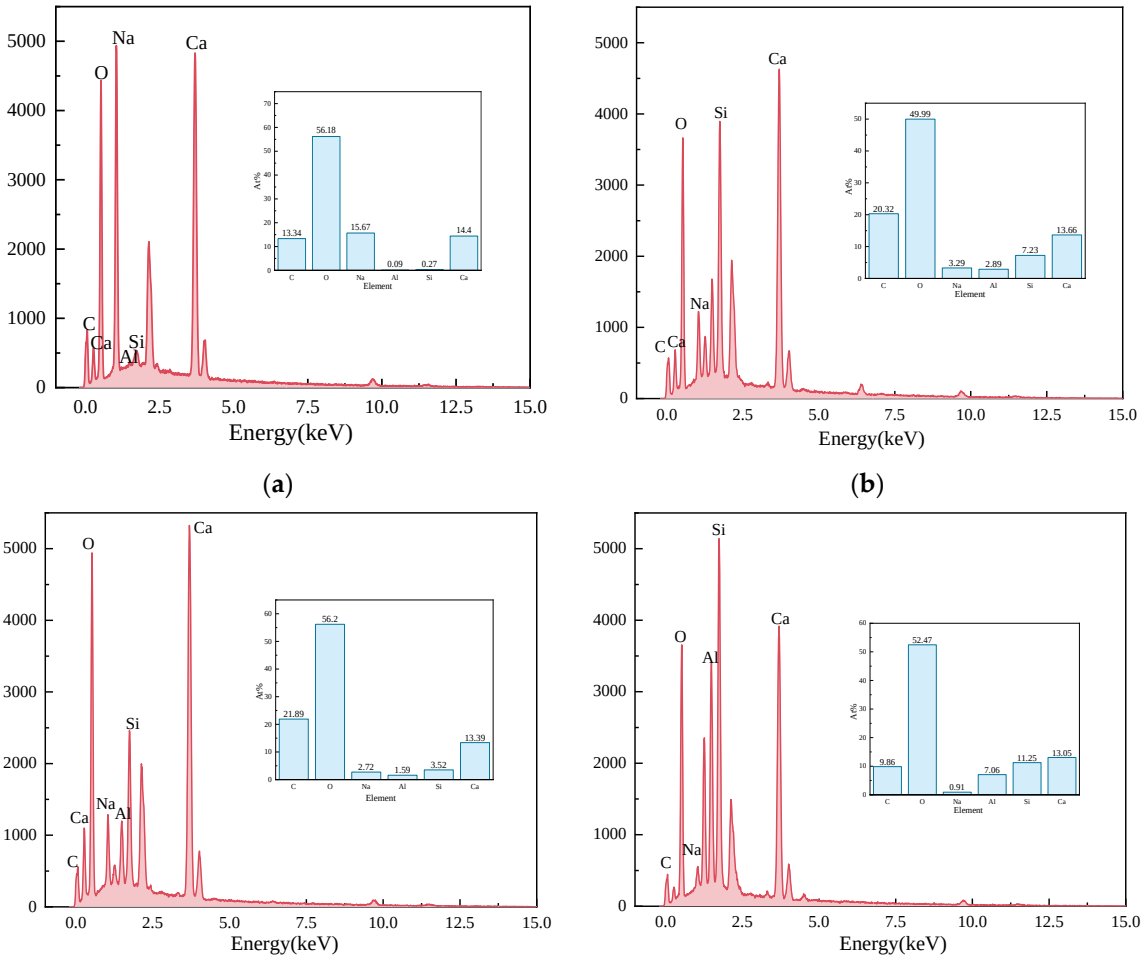

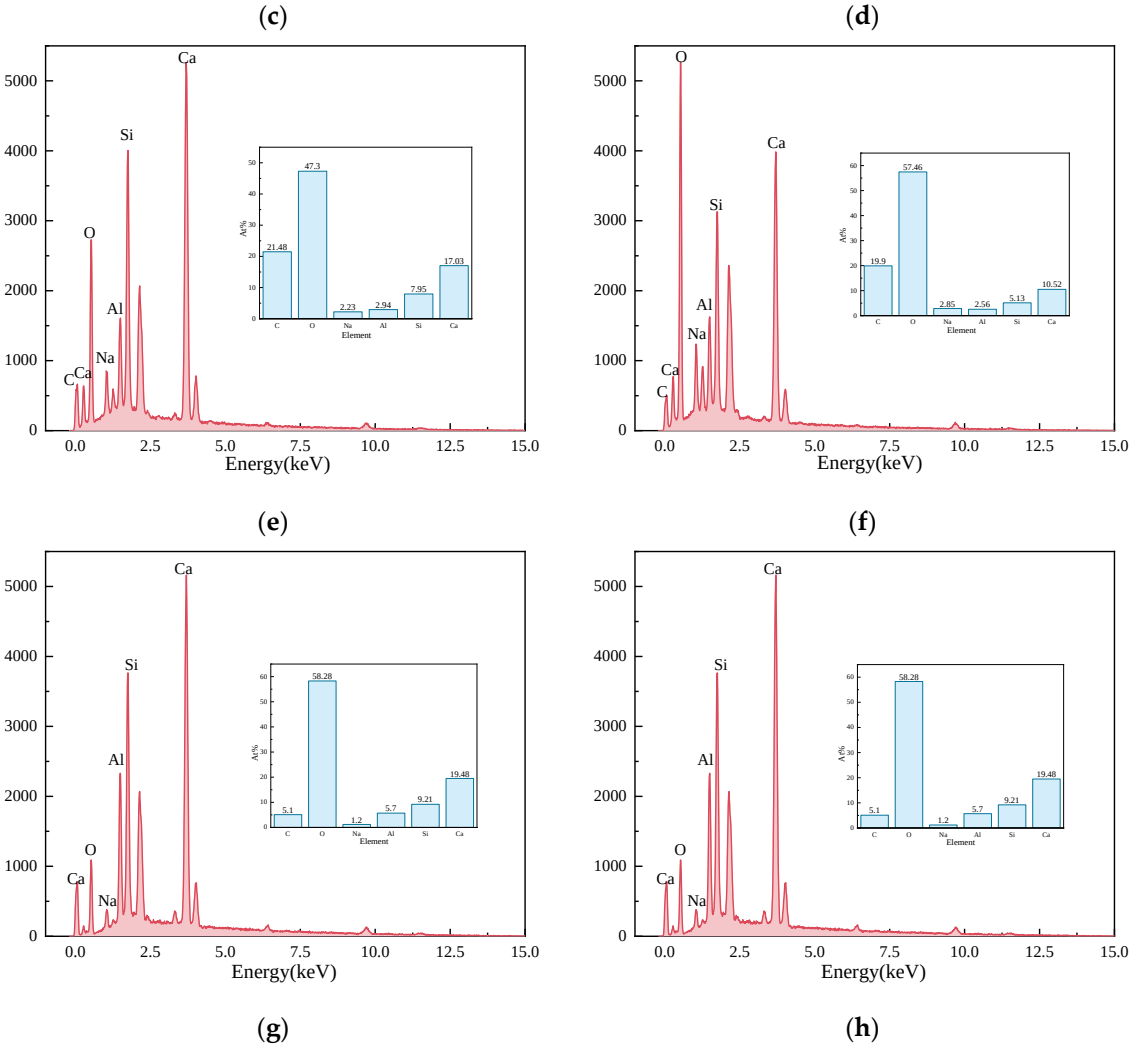

Figure 11. EDS results for the points in sample S50F30C20 in Figure 10d : (**a**) EDS point 1; (**b**) EDS point 2; (**c**) EDS point 3; (**d**) EDS point 4; (**e**) EDS point 5; (**f**) EDS point 6; (**g**) EDS point 7; (**h**) EDS point 8.

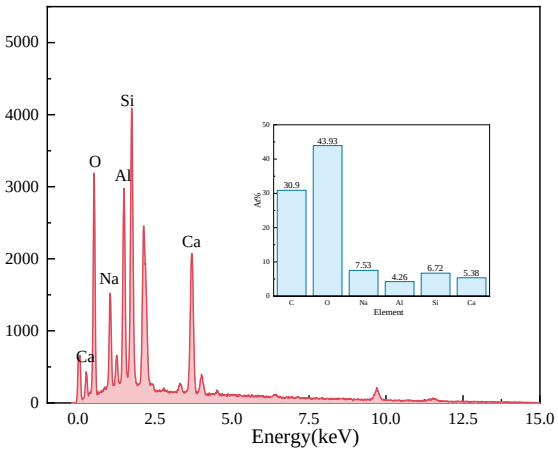

Figure 12. Elemental analysis of the microstructure of sample S50F50C0 Figure 10a.

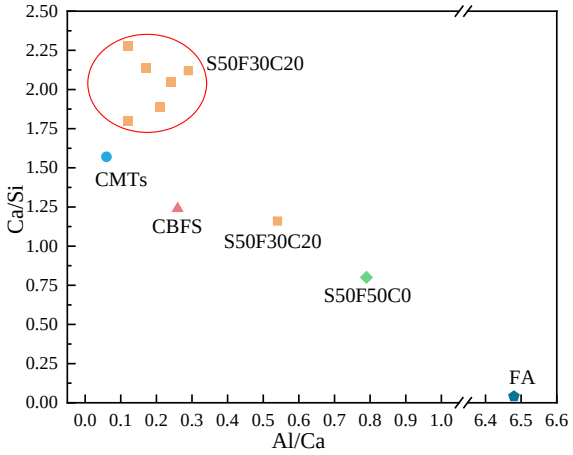

Figure 13. The Ca/Si and Ca/Al atomic ratios of sample S50F30C20, sample S50F50C0, and the raw materials.

After 28 days of curing, the microstructure and surface scanning results of the AASFCS paste mixture sample S50F30C20, which exhibited the best compressive strength, are shown in Figure 14. The varying brightness of regions represents different content levels of elemental distribution, with brighter areas indicating higher elemental content.

By calculation, the Ca/Si atomic ratio in Figure 14a turned out to be 2.83, which was much higher than that of sample S50F50C0, which showed that the addition of CMTs had increased the calcium component, consistent with the EDS point scan analysis results. The percentage of calcium atoms in the sample was the highest compared to the percentages of sodium, aluminum, and silicon atoms, and the uniform distribution of calcium in the sample suggested that calcium was present in all the minerals. The uniform distribution of silicon, aluminum, and oxygen represented the distribution of hydration products such as C(-A)-S-H gels in the sample. The uneven distribution of sodium suggested the non-uniformity of the activating effect of the modified sodium silicate, indicating that further research was needed to improve the uniform action of the alkali activator.

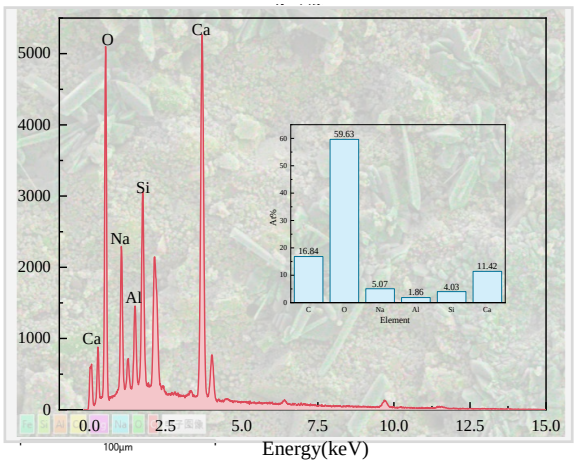

(**a**)

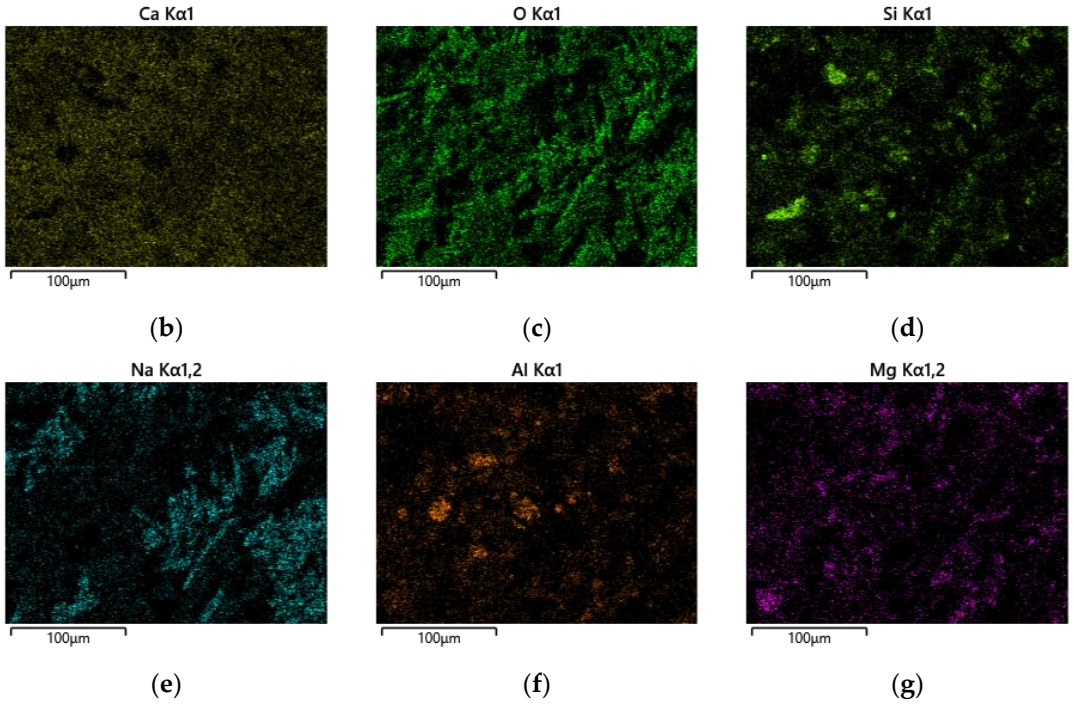

Figure 14. Microstructure and surface scans of sample S50F30C20: (**a**) elemental analysis results; (**b**) Ca; (**c**) O; (**d**) Si; (**e**) Na; (**f**) Al; (**g**) Mg.

4. Conclusions

CMTs demonstrate promising application potential in the field of alkali-activated cementitious materials, and this paper aims to provide a rationalized technical approach and data support for the preparation of cementitious materials from CMTs. The study investigates the influence of CMTs on the compressive strength of AASFCS. Based on the experimental results, the following conclusions could be drawn:

1. The AASFCS paste with the incorporation of CMTs, S50F30C20 (50% GBFS, 30% FA, 20% CMTs), achieved the highest 28 d compressive strength, achieving up to 79.14 MPa. When the CBFS content was kept constant, varying the amounts of FA and CMTs affected the compressive strength of the samples in the range of 8% to 20%, with samples containing different amounts of CMTs showing similar strength development. When the CMTs content was constant, the compressive strength of the specimens increased with the increase in the amount of CBFS.
2. FTIR spectroscopy and XRD analysis indicated that the reaction products of AASFCS mainly included ettringite, quartz, C(-N)-S-H gel, and calcite, with the presence of CMTs leading to the formation of the complex salt phase gaylussite. TG-DTG results once again confirmed the types of reaction products in AASFCS, with an increasing trend in the mass of chemically bound water in hydration products after the addition of CMTs.
3. SEM and EDS results showed that the presence of CMTs increases the calcium element in the hydration products, significantly affecting the morphological characteristics of the hydration products. Under the optimal proportion conditions of AASFCS, the reaction products formed a continuous and unified whole, resulting in a denser microstructure. Excessive CMTs particles might restrict the growth of the hydration gel, leading to poor continuity and more micro-defects in the samples, which exhibit lower compressive strength.
4. CMTs in AASFCS might improve the compressive strength due to both filling effects and participation in chemical reactions. On the one hand, the fine particles in CMTs

provided additional nucleation sites that promoted the formation of hydration products, thereby leading to a slight increase in compressive strength. On the other hand, the increase in compressive strength might be attributed to the release of Ca^{2+} from CMTs under the action of alkaline solutions, which participated in the reactions.

It is necessary to acknowledge the limitations of this work. As this research focuses on the influence of CMTs on the compressive strength of AASFCS, the role played by sodium silicate and type of cementitious material in strength development was not specifically analyzed, and other properties of CMTs alkali-activated cementitious materials were not captured, which may affect the applicability of CMTs alkali-activated cementitious materials. In the next study, the influence of CMTs on the setting time, fluidity, and shrinkage properties of alkali-activated cementitious materials will be explored, and the influence of sodium silicate on the reaction mechanism of CMTs will be investigated. Given the high calcium content of CMTs, further research on the reaction mechanism and basic properties of other high-calcium alkali-activated cementitious materials with CMTs will be considered to provide theoretical basis and technical support for large-scale practical application.

Author Contributions: Conceptualization, X.X.; methodology, J.L.; formal analysis, F.W.; investigation, Y.Z.; data curation, F.W.; writing—original draft preparation, F.W.; writing—review and editing, X.G.; supervision, Q.W.; funding acquisition, X.G. All authors have read and agreed to the published version of the manuscript.

Funding: This research was funded by the National Key Research and Development Plan of China grant number No. 2023YFC3904303, the National Natural Science Foundation of China grant number No. 52234004, and the Social Governance Special Project of Shenyang Municipal Bureau of Science and Technology grant number No. 22-322-3-02.

Data Availability Statement: Data are contained within the article.

Conflicts of Interest: The authors declare no conflict of interest.

References

1. Liu, Y.; Zheng, Y.; Wang, Y.; Ren, P.; Sun, B.; Gao, F.; Gong, X. Life cycle assessment of beneficial use of calcium carbide sludge in cement clinker production: A case study in China. *J. Clean Prod.* **2023**, *418*, 138003. https://doi.org/10.1016/j.jclepro.2023.138003.
2. Dobiszewska, M.; Bagcal, O.; Beycioğlu, A.; Goulias, D.; Köksal, F.; Płomiński, B.; Ürünveren, H. Utilization of rock dust as cement replacement in cement composites: An alternative approach to sustainable mortar and concrete productions. *J. Build. Eng.* **2023**, *69*, 106180. https://doi.org/10.1016/j.jobe.2023.106180.
3. Xiang, Q.; Pan, H.; Ma, X.; Yang, M.; Lyu, Y.; Zhang, X.; Shui, W.; Liao, W.; Xiao, Y.; Wu, J.; et al. Impacts of energy-saving and emission-reduction on sustainability of cement production. *Renew. Sustain. Energy Rev.* **2024**, *191*, 114089. https://doi.org/10.1016/j.rser.2023.114089.
4. Zhao, J.; Li, S. Study on processability, compressive strength, drying shrinkage and evolution mechanisms of microstructures of alkali-activated slag-glass powder cementitious material. *Constr. Build. Mater.* **2022**, *344*, 128196. https://doi.org/10.1016/j.conbuildmat.2022.128196.
5. Sahoo, N.; Kumar, A.; Samsher. Design of solar cement plant for supplying thermal energy in cement production. *J. Clean Prod.* **2023**, *426*, 139151. https://doi.org/10.1016/j.jclepro.2023.139151.
6. Gallego Dávila, J.; Sacchi, R.; Pizzol, M. Preconditions for achieving carbon neutrality in cement production through CCUS. *J. Clean Prod.* **2023**, *425*, 138935. https://doi.org/10.1016/j.jclepro.2023.138935.
7. Sahoo, N.; Kumar, A.; Samsher. Potential of solar thermal calciner technology for cement production in India and consequent carbon mitigation. *Process Saf. Environ. Prot.* **2023**, *179*, 667–676. https://doi.org/10.1016/j.psep.2023.09.041.
8. Luo, Q.; Li, P.; Cai, L.; Zhou, P.; Tang, D.; Zhai, P.; Zhang, Q. A Thermoelectric Waste-Heat-Recovery System for Portland Cement Rotary Kilns. *J. Electron. Mater.* **2014**, *44*, 1750–1762. https://doi.org/10.1007/s11664-014-3543-1.
9. Madlool, N.A.; Saidur, R.; Hossain, M.S.; Rahim, N.A. A critical review on energy use and savings in the cement industries. *Renew. Sustain. Energy Rev.* **2011**, *15*, 2042–2060. https://doi.org/10.1016/j.rser.2011.01.005.
10. Sun, B.; Ye, G.; de Schutter, G. A review: Reaction mechanism and strength of slag and fly ash-based alkali-activated materials. *Constr. Build. Mater.* **2022**, *326*, 126843. https://doi.org/10.1016/j.conbuildmat.2022.126843.
11. Li, X.; Gu, X.; Liu, B.; Li, Z.; Zhang, W.; Liu, J.; Nehdi, M.L. Evaluation of waste powder from open pit mines as supplementary cementitious material: Crystal structure and hydration characteristics. *J. Build. Eng.* **2023**, *71*, 106514. https://doi.org/10.1016/j.jobe.2023.106514.

12. Zhang, W.; Gu, X.; Qiu, J.; Liu, J.; Zhao, Y.; Li, X. Effects of iron ore tailings on the compressive strength and permeability of ultra-high performance concrete. *Constr. Build. Mater.* **2020**, *260*, 119917. https://doi.org/10.1016/j.conbuildmat.2020.119917.
13. Du, Z.; Ge, L.; Ng, A.H.-M.; Zhu, Q.; Horgan, F.G.; Zhang, Q. Risk assessment for tailings dams in Brumadinho of Brazil using InSAR time series approach. *Sci. Total Environ.* **2020**, *717*, 137125. https://doi.org/10.1016/j.scitotenv.2020.137125.
14. Felekoglu, B. Utilisation of high volumes of limestone quarry wastes in concrete industry (self-compacting concrete case). *Resour. Conserv. Recycl.* **2007**, *51*, 770–791. https://doi.org/10.1016/j.resconrec.2006.12.004.
15. Tang, Z.; Zhang, Q.; Sun, Y.; Gao, P.; Han, Y. Pilot-scale extraction of iron from flotation tailings via suspension magnetization roasting in a mixture of CO and H_2 followed by magnetic separation. *Resour. Conserv. Recycl.* **2021**, *172*, 105680. https://doi.org/10.1016/j.resconrec.2021.105680.
16. Saedi, A.; Jamshidi-Zanjani, A.; Mohseni, M.; Khodadadi Darban, A.; Nejati, H. Mechanical activation of lead–zinc mine tailings as a substitution for cement in concrete construction. *Constr. Build. Mater.* **2023**, *364*, 129973. https://doi.org/10.1016/j.conbuildmat.2022.129973.
17. Xie, R.; Ge, R.; Li, Z.; Qu, G.; Zhang, Y.; Xu, Y.; Zeng, Y.; Li, Z. Synthesis and influencing factors of high-performance concrete based on copper tailings for efficient solidification of heavy metals. *J. Environ. Manag.* **2023**, *325*, 116469. https://doi.org/10.1016/j.jenvman.2022.116469.
18. Sun, B.; Sun, Y.; Ye, G.; De Schutter, G. A mix design methodology of slag and fly ash-based alkali-activated paste. *Cem. Concr. Compos.* **2022**, *126*, 104368. https://doi.org/10.1016/j.cemconcomp.2021.104368.
19. Abdulkareem, M.; Havukainen, J.; Nuortila-Jokinen, J.; Horttanainen, M. Environmental and economic perspective of waste-derived activators on alkali-activated mortars. *J. Clean Prod.* **2021**, *280*, 124651. https://doi.org/10.1016/j.jclepro.2020.124651.
20. Puertas, F.; González-Fonteboa, B.; González-Taboada, I.; Alonso, M.M.; Torres-Carrasco, M.; Rojo, G.; Martínez-Abella, F. Alkali-activated slag concrete: Fresh and hardened behaviour. *Cem. Concr. Compos.* **2018**, *85*, 22–31. https://doi.org/10.1016/j.cemconcomp.2017.10.003.
21. Yazdi, M.A.; Liebscher, M.; Hempel, S.; Yang, J.; Mechtcherine, V. Correlation of microstructural and mechanical properties of geopolymers produced from fly ash and slag at room temperature. *Constr. Build. Mater.* **2018**, *191*, 330–341. https://doi.org/10.1016/j.conbuildmat.2018.10.037.
22. Stefanini, L.; Ghorbani, S.; De Schutter, G.; Matthys, S.; Walkley, B.; Provis, J.L. Evaluation of copper slag and stainless steel slag as replacements for blast furnace slag in binary and ternary alkali-activated cements. *J. Mater. Sci.* **2023**, *58*, 12537–12558. https://doi.org/10.1007/s10853-023-08815-7.
23. Huang, G.; Zhang, X.; Liu, M.; Fang, B.; Wang, C.; Mi, H. Compatibility of sodium hydroxide, sodium silicate and calcium-enriched additives in alkali-activated materials: From the perspectives of flowability, strength and microstructure. *Constr. Build. Mater.* **2023**, *403*, 133102. https://doi.org/10.1016/j.conbuildmat.2023.133102.
24. Liu, J.; Ge, X.; Liu, P.; Song, G.; Hu, Z. Experimental study on the preparation of cementitious materials from iron ore tailings by activation. *Constr. Build. Mater.* **2023**, *385*, 131409. https://doi.org/10.1016/j.conbuildmat.2023.131409.
25. Sumajouw, D.M.J.; Hardjito, D.; Wallah, S.E.; Rangan, B.V. Fly ash-based geopolymer concrete: Study of slender reinforced columns. *J. Mater. Sci.* **2006**, *42*, 3124–3130. https://doi.org/10.1007/s10853-006-0523-8.
26. Ramagiri, K.K.; Kar, A. Environmental impact assessment of alkali-activated mortar with waste precursors and activators. *J. Build. Eng.* **2021**, *44*, 103391. https://doi.org/10.1016/j.jobe.2021.103391.
27. Shi, C.; Jiménez, A.F.; Palomo, A. New cements for the 21st century: The pursuit of an alternative to Portland cement. *Cem. Concr. Res.* **2011**, *41*, 750–763. https://doi.org/10.1016/j.cemconres.2011.03.016.
28. Provis, J.L.; Palomo, A.; Shi, C. Advances in understanding alkali-activated materials. *Cem. Concr. Res.* **2015**, *78*, 110–125. https://doi.org/10.1016/j.cemconres.2015.04.013.
29. Xiang, J.; Qiu, J.; Zhao, Y.; Zheng, P.; Peng, H.; Fei, X. Rheology, mechanical properties, and hydration of synergistically activated coal gasification slag with three typical solid wastes. *Cem. Concr. Compos.* **2024**, *147*, 105418. https://doi.org/10.1016/j.cemconcomp.2023.105418.
30. Brough, A.R.; Atkinson, A. Sodium silicate-based, alkali-activated slag mortars Part I. Strength, hydration and microstructure. *Cem. Concr. Res.* **2002**, *32*, 865–879. https://doi.org/10.1016/S0008-8846(02)00717-2.
31. Ghorbani, S.; Stefanini, L.; Sun, Y.; Walkley, B.; Provis, J.L.; De Schutter, G.; Matthys, S. Characterisation of alkali-activated stainless steel slag and blast-furnace slag cements. *Cem. Concr. Compos.* **2023**, *143*, 105230. https://doi.org/10.1016/j.cemconcomp.2023.105230.
32. Sarıdemir, M.; Bulut, M.; Akça, U. Effects of different curing conditions on the long-term properties of alkali activated GBP + GBFS mortars exposed to high temperatures. *Constr. Build. Mater.* **2022**, *321*, 125732. https://doi.org/10.1016/j.conbuildmat.2021.125732.
33. Bayat, A.; Hassani, A.; Yousefi, A.A. Effects of red mud on the properties of fresh and hardened alkali-activated slag paste and mortar. *Constr. Build. Mater.* **2018**, *167*, 775–790. https://doi.org/10.1016/j.conbuildmat.2018.02.105.
34. Gao, X.; Yu, Q.L.; Brouwers, H.J.H. Properties of alkali activated slag–fly ash blends with limestone addition. *Cem. Concr. Compos.* **2015**, *59*, 119–128. https://doi.org/10.1016/j.cemconcomp.2015.01.007.
35. Perumal, P.; Niu, H.; Kiventerä, J.; Kinnunen, P.; Illikainen, M. Upcycling of mechanically treated silicate mine tailings as alkali activated binders. *Miner. Eng.* **2020**, *158*, 106587. https://doi.org/10.1016/j.mineng.2020.106587.

36. Falah, M.; Ohenoja, K.; Obenaus-Emler, R.; Kinnunen, P.; Illikainen, M. Improvement of mechanical strength of alkali-activated materials using micro low-alumina mine tailings. *Constr. Build. Mater.* **2020**, *248*, 118659. https://doi.org/10.1016/j.conbuildmat.2020.118659.
37. Tian, X.; Zhang, H.; Zhang, T.; Fernández, C.A. Alkali-activated copper tailings-based pastes: Compressive strength and microstructural characterization. *J. Mater. Res. Technol.* **2020**, *9*, 6557–6567. https://doi.org/10.1016/j.jmrt.2020.04.043.
38. Obenaus-Emler, R.; Falah, M.; Illikainen, M. Assessment of mine tailings as precursors for alkali-activated materials for on-site applications. *Constr. Build. Mater.* **2020**, *246*, 118470. https://doi.org/10.1016/j.conbuildmat.2020.118470.
39. Zhang, Y.; Liu, H.; Ma, T.; Chen, C.; Gu, G.; Wang, J.; Shang, X. Experimental assessment of utilizing copper tailings as alkali-activated materials and fine aggregates to prepare geopolymer composite. *Constr. Build. Mater.* **2023**, *408*, 133751. https://doi.org/10.1016/j.conbuildmat.2023.133751.
40. Wang, C.; Chen, P.; Wang, C. Investigation on the basic performance of the sustainable alkali-activated slag blended with sulphidic copper tailings. *Case Stud. Constr. Mater.* **2024**, *20*, e02844. https://doi.org/10.1016/j.cscm.2023.e02844.
41. Yang, Y.; Zhang, J.; Fu, Y.; Long, W.; Dong, B. Synthesis of one-part geopolymers from alkaline-activated molybdenum tailings: Mechanical properties and microstructural evolution. *J. Clean Prod.* **2024**, *443*, 141129. https://doi.org/10.1016/j.jclepro.2024.141129.
42. Cheng, Y.; Qi, R.; Hou, J.; Huang, Q. Feasibility study on utilization of copper tailings as raw meal and addition for low carbon Portland cement production. *Constr. Build. Mater.* **2023**, *382*, 131275. https://doi.org/10.1016/j.conbuildmat.2023.131275.
43. Yu, R.; Dong, E.; Shui, Z.; Qian, D.; Fan, D.; Wang, J.; Leng, Y.; Liu, K.; Chen, Z. Advanced utilization of molybdenum tailings in producing Ultra High-Performance Composites based on a green activation strategy. *Constr. Build. Mater.* **2022**, *330*, 127272. https://doi.org/10.1016/j.conbuildmat.2022.127272.
44. Zhang, W.; Liu, X.; Zhang, Z.; Li, Y.; Gu, J.; Wang, Y.; Xue, Y. Circulating fluidized bed fly ash-blast furnace slag based cementitious materials: Hydration behaviors and performance. *Constr. Build. Mater.* **2022**, *342*, 128006. https://doi.org/10.1016/j.conbuildmat.2022.128006.
45. Nguyen, T.H.Y.; Tsuchiya, K.; Atarashi, D. Microstructure and composition of fly ash and ground granulated blast furnace slag cement pastes in 42-month cured samples. *Constr. Build. Mater.* **2018**, *191*, 114–124. https://doi.org/10.1016/j.conbuildmat.2018.09.206.
46. Lemougna, P.N.; Wang, K.-t.; Tang, Q.; Cui, X.-m. Study on the development of inorganic polymers from red mud and slag system: Application in mortar and lightweight materials. *Constr. Build. Mater.* **2017**, *156*, 486–495. https://doi.org/10.1016/j.conbuildmat.2017.09.015.
47. Wang, S.; Gu, X.; Liu, J.; Zhu, Z.; Wang, H.; Ge, X.; Xu, X.; Nehdi, M.L. Modulation of the workability and Ca/Si/Al ratio of cement-metakaolin cementitious material system by using fly ash: Synergistic effect and hydration products. *Constr. Build. Mater.* **2023**, *404*, 133300. https://doi.org/10.1016/j.conbuildmat.2023.133300.
48. Huseien, G.F.; Sam, A.R.M.; Shah, K.W.; Asaad, M.A.; Tahir, M.M.; Mirza, J. Properties of ceramic tile waste based alkali-activated mortars incorporating GBFS and fly ash. *Constr. Build. Mater.* **2019**, *214*, 355–368. https://doi.org/10.1016/j.conbuildmat.2019.04.154.
49. Kumar, S.; García-Triñanes, P.; Teixeira-Pinto, A.; Bao, M. Development of alkali activated cement from mechanically activated silico-manganese (SiMn) slag. *Cem. Concr. Compos.* **2013**, *40*, 7–13. https://doi.org/10.1016/j.cemconcomp.2013.03.026.
50. Zhao, Y.; Gu, X.; Xu, X.; Zhang, Z. Using calcium carbide residue to prepare ecological alkali activated slag composites: Effect of anion type. *Ceram. Int.* **2023**, *49*, 25092–25104. https://doi.org/10.1016/j.ceramint.2023.05.039.
51. Cota, T.G.; Cheloni, L.M.d.M.S.; Guedes, J.J.M.; Reis, É.L. Silico-manganese slag and its utilization into alkali-activated materials: A critical review. *Constr. Build. Mater.* **2023**, *399*, 132589. https://doi.org/10.1016/j.conbuildmat.2023.132589.
52. Hasnaoui, A.; Bourguiba, A.; El Mendili, Y.; Sebaibi, N.; Boutouil, M. A preliminary investigation of a novel mortar based on alkali-activated seashell waste powder. *Powder Technol.* **2021**, *389*, 471–481. https://doi.org/10.1016/j.powtec.2021.05.069.
53. Wang, T.; Qiu, X.; Yang, W.; Ma, C. Study on properties and mechanism of alkali-activated geopolymer cementitious materials of marble waste powder. *Dev. Built Environ.* **2023**, *16*, 100249. https://doi.org/10.1016/j.dibe.2023.100249.
54. Wang, H.; Gu, X.; Liu, J.; Zhu, Z.; Wang, S.; Xu, X.; Meng, J. Enhancement mechanism of micro-iron ore tailings on mechanical properties and hydration characteristics of cement-steel slag system. *J. Build. Eng.* **2023**, *79*, 107882. https://doi.org/10.1016/j.jobe.2023.107882.
55. Srinivas, D.; Ramagiri, K.K.; Kar, A.; Adak, D.; Noroozinejad Farsangi, E.; Dutta, S. Experimental characterization of quaternary blended mortar exposed to marine environment using mechanical strength, corrosion resistance and chemical composition. *J. Build. Eng.* **2021**, *42*, 102822. https://doi.org/10.1016/j.jobe.2021.102822.
56. Aydın, S.; Baradan, B. Mechanical and microstructural properties of heat cured alkali-activated slag mortars. *Mater. Des.* **2012**, *35*, 374–383. https://doi.org/10.1016/j.matdes.2011.10.005.